Science Advances
AAAS

Supplementary Materials for

In situ diagnosis and simultaneous treatment of cardiac diseases using a single-device platform

Jae Chul Hwang *et al.*

Corresponding author: Jang-Ung Park, jang-ung@yonsei.ac.kr; Sak Lee, sak911@yuhs.ac.kr; Seung-Woo Cho, seungwoocho@yonsei.ac.kr

Sci. Adv. **8**, eabq0897 (2022)
DOI: 10.1126/sciadv.abq0897

The PDF file includes:

Other Supplementary Material for this manuscript includes the following:

Supplementary Text

Fabrication of flexible heart-attachable, patch-type device platform

1. Preparation of flexible substrate

To fabricate a flexible polyimide (PI) substrate, colorless polyamic acid varnish (viscosity: 11,200 mPa.S) was spin-coated on a bare Si wafer at 1,000 rpm, 30 sec (8 μm thickness for bottom substrate) and 2,500 rpm, 30 sec (3 μm for top substrate). After spin-coating procedure, the bottom and top PI substrates were undergone step by step thermal imidization in a convection oven. (150 °C for 10min, 180 °C for 10 min, 210 °C for 10 min, 250 °C for 10 min, 300 °C for 10 min)

2. Fabrication of flexible pressure sensor with integrated pacing electrode

The flexible pressure sensor was formed through an assembly of bottom and top panel which is composed of transistor array and pacing electrode, respectively. The bottom panel was first fabricated by transferring single-crystalline Si layer (160 nm) onto a flexible substrate. The procedures to transfer the Si channels onto the transparent PI substrate (thickness: 8 μm) are as follows. First, array of silicon channels was photolithographically patterned using positive photoresist (S1818, MicroChem) on SOI wafer (silicon-on-insulator, 160 nm Si on 400 nm buried oxide, Soitec). The Si channels (channel length: 40 μm, width: 150 μm) were etched with reactive ion etching (RIE) system with sulphur hexafluoride plasma (SF_6 25 sccm / Ar 55 sccm, 300 W / 40 sec), completing the channel isolation process. Any photoresist residue left was subsequently removed through Piranha solution (10 min). To separate the Si channel from the SOI wafer, the buried oxide layer was etched in 50% HF solution (18 min). The isolated Si channels were then transferred onto the bottom PI substrate using polydimethylsiloxane (PDMS) stamping method. Then, metal layers were deposited (Cr 5 nm / Au 100 nm) onto the Si/PI substrate by e-beam evaporation. The source, drain, and interconnect electrodes were then fabricated by photolithographically patterning it with positive photoresist S1818 and etching it with gold and chrome etchant. A negative photoresist (SU-8 2020, MicroChem) was photolithographically patterned at 1 μm of thickness to define the air-dielectric area and passivate the patterned metal electrodes. The sample was then rinsed with IPA and distilled water and was subsequently dried with N_2 gas.

To fabricate the top panel of the device, metal layers were deposited (Cr 5 nm / Au 100 nm) onto a thin PI film (thickness: 3 μm) which was thermally imidized on a bare Si wafer. The metallic layers of substrate were etched using the same previous methods to fabricate the gate electrode. To fabricate the pressure-sensitive air-dielectric layer, PDMS solution (10:1 weight ratio of base and curing agent) was spin-coated at (1500 rpm, 30 sec, 25 μm thickness) on a release film and cured at 40 °C for 4 hours. The top surface of the PDMS was pre-perforated using laser ablation method (CO_2 laser, Epilog Laser, Inc) to clearly define the air-vacant holes. The air-dielectric elastomeric layer was completed by aligning PDMS layer using alignment keys with the gate film, which was treated with O_2 plasma using reactive-ion-etching (RF power of 50W, working pressure of 200 mTorr, 30 seconds, 25 sccm O_2) to improve surface adhesion. It was then cured at 60 °C for 4 hours.

To remove residual water vapor before the assembling process, each panel was thermally treated at 100 ℃ for 30 min on a hotplate. Each fabricated panel was cut into the desired shape and then peeled off from the bare Si wafer. The bottom panel (Si channel, source, drain electrodes) and the top panel (air dielectric elastomeric layer, gate electrode) were precisely aligned using

alignment keys and laminated in a vacuum condition. The entire side walls of completed device was coated with biomedical grade silicone elastomer (Silastic MDX4-4210, Dow Inc., base : curing agent = 10 : 1) using diluted biomedical grade silicone fluid (viscosity: 20 cSt). The elastomer was cured at 40 °C for 24 hours. Subsequently, a 100 nm-thick parylene encapsulation layer (as a biocompatible insulating layer) was deposited on the top surface of this sample by chemical vapor deposition (CVD).

3. Fabrication of pacing electrodes

To fabricate a pair of pacing electrodes (ground and stimulation, respectively), Cr/Au (5 nm/60 nm) electrodes were deposited on the outer side of the top gate film by e-beam evaporator using a designed shadow mask. Pt black nanoparticles were subsequently formed via electroplating technique. Experimental procedures reported in Stanca et al. research were used for Pt black electroplating (*71*). The electroplating setup consists of a classical electrolysis cell with an electrolyte bath and two electrodes. Pt wire acts as an anode in the electrolysis cell and the Cr/Au pacing electrode acted as a cathode. The electrolyte was prepared with 0.5 g of platinum salt (Platinum IV chloride: $PtCl_4$) and 0.01 g of $Pb(CH_3COO)_2$ dissolved in 50 mL of distilled water. To completely dissolve the salt, the electrolytic bath was sonicated for 30 min. It was then filtrated through the membrane filter (Porafil, pore size 450 μm) to remove undissolved Pt salt and any additional $PbCl_2$ salt. The duration of electrolysis time was 60 s and was conducted under an electrical current density of 0.1 A/cm^2. Finally, a parylene layer was deposited (500 nm thickness) with a shadow mask to insulate the area of the electrode other than the pacing site.

4. Connection to signal processing module

To connect the fabricated pressure sensor array in this device platform to a signal processing module, contact pads of the bottom and top panel were connected to extend interconnect films, which were fabricated with metal interconnects formed on both sides, using anisotropic conducting paste (ACP), respectively. Next, a custom-made flexible flat cable (FFC), which links to the signal processing module, was connected to the extended interconnect film using anisotropic conducting film (ACF). The pacing electrodes were connected by FFC to the external pulse generator.

Device characterization

The transfer and output characteristics of transistors were characterized using a probe station (Keithley 4200-SCS). To measure their pressure responsive properties, compressive pressures were applied using a high-precision, motorized Z-stage (Mark-10 ESM303) with a force gauge (Mark-10 M7-20) or by placing different weights on the transistors. The spatiotemporal mapping of pressure distribution was calculated by measuring the relative change in I_D ($\Delta I_D/I_0$) of each transistor before and after applying pressures. For the application of electrical impulses, FFC film was used to connect the pacing electrodes to a pulse generator.

Data acquisition

The DAQ system, which collected a real time pressure distribution data, consisted of a set of two sourcemeters (Keithley 2400), system switch (Keithley 3706), relay card (Keithley 3723) and custom LabVIEW software. Our active-matrix pressure-sensitive transistor array was connected to two sourcemeters using IEE-488 GPIB (General Purpose Interface Bus), to control drain and

gate voltages of each pixel. A USB to GPIB interface converter (Keithley KUSB-488B) was used to communicate readouts between the laptop computer and data control instruments (Keithley 3723). Also, the laptop computer was connected by a system switch module (Keithley 3706) using a LAN cable. Custom LabVIEW-based software controlled the DAQ system and visualized output signal at a sampling frequency of 1kHz.

Formation of an artificial heart

The artificial hearts were formed by compressive molding method using the low modulus silicone elastomer (Ecoflex 0030, Smooth-on, Inc.). The upper and lower molds with varying wall thickness were created by the 3D printer (DP 201, Sindoh, Co., Korea) using polylactic acid (PLA) material. The Ecoflex silicone elastomer mixed parts A and B (1:1 ratio) was poured into the lower mold and closed upper mold by compression force of ~ 1MPa, following cured at 40 ℃ for 24 hours. The artificial blood injected into the artificial heart was prepared by dissolving red dye (Allura red, Sigma-Aldrich) in water.

Synthesis of Alg-CA conjugate

The alginate-catechol (Alg-CA) conjugate was synthesized by conjugating amine group of dopamine to carboxyl groups of alginate backbone via carbodiimide coupling chemistry as previously reported (*72*). Briefly, alginate polymer (Pronatal LF10/60, FMC Biopolymer, Philadelphia, PA, USA) was dissolved in triple distilled water (TDW) at a concentration of 10 mg/ml. 1-(3-Dimethylaminopropyl)-3-ethylcarbodiimide hydrochloride (EDC; Tokyo Chemical Industry Co., Ltd., Tokyo, Japan) and N-hydroxysulfosuccinimide (NHS; Sigma-Aldrich, St. Louis, MO, USA) were added to the alginate solution at an equal molar ratio to alginate and reacted for 30 minutes at pH < 7. Then, dopamine hydrochloride (Sigma-Aldrich) was added to the reaction solution at an equimolar ratio to alginate and reacted for 24 hours at room temperature maintaining pH 5 using 1 M hydrochloride. The reaction mixture was dialyzed using a dialysis membrane (Cellu Sep T2, MW cut-off 6-8 kDa; Membrane Filtration Products Inc., Seguin, TX, USA) against acidic phosphate-buffered saline (acidic PBS, pH 4.3; Biosesang, Seongnam, Korea) and TDW for 24 hours to remove unreacted chemical and byproducts. The synthesized product was lyophilized and stored in a refrigerator until use. To form a bulk Alg-CA hydrogel, the lyophilized Alg-CA conjugate was dissolved in phosphate-buffered saline (PBS, pH 7~7.4; Sigma-Aldrich) and mixed with an oxidizing solution containing 4.5 mg/ml of $NaIO_4$ (Sigma-Aldrich) and 0.5 M NaOH, producing the hydrogels at final concentrations of 2 and 4% (w/v).

Rheological analysis of Alg-CA-Ca^{2+} adhesive layer

All rheological analyses were performed using a model MCR 102 rheometer (Anton Paar, Ashland, VA, USA). The storage modulus (G′) and loss modulus (G″) of the adhesive patches crosslinked by using crosslinking agents with different concentrations of $CaCl_2$ and a fixed concentration of $NaIO_4$ were measured in a frequency sweep mode at a frequency range of 0.1 to 10 Hz. The elastic modulus of the hydrogel was determined by calculating the average storage modulus of each hydrogel at 1 Hz (n = 5). The elasticity (tan δ) of the adhesive patches was calculated by dividing the loss modulus by storage modulus (G″/G′) at 1 Hz (n = 5). The

mechanical stability test of Alg-CA-Ca^{2+} adhesive layer was performed using a rheometer (MCR102) in a fixed frequency (2.5 Hz) and oscillatory tensile strain (30 %) mode for 30 minutes.

Measurement of tissue adhesion strengths of Alg-CA-Ca^{2+} adhesive layer

The tissue adhesion strengths of the Alg-CA-Ca^{2+} patches to porcine heart tissue were measured using a rheometer (MCR102) in a tack test mode. Porcine heart tissues were fixed onto the surfaces of the base plate and probe using a conventional acrylic glue to assess the tissue adhesiveness of the Alg-CA patches with and without Ca^{2+}. Tack tests were performed in a pull-off manner, pulling the probe at 10 µm/s. The work of adhesion was measured by calculating the area under the force-displacement curve (n = 5).

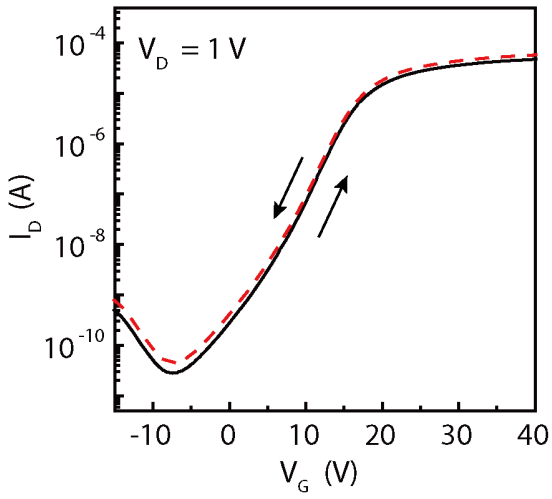

Fig. S1. Transfer characteristics. Negligible hysteresis of the pressure-sensitive air-dielectric transistor of the epicardial patch device.

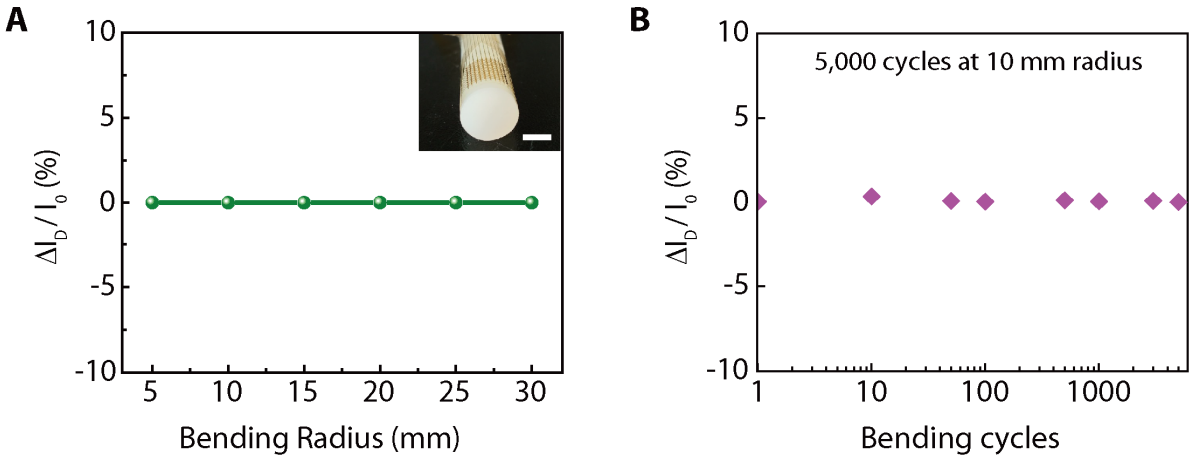

Fig. S2. Bending endurance test of the patch-type device platform. (**A**) The change in the transistor signal ($\Delta I_D/I_0$) with respect to bending radius from 5 mm to 30 mm which corresponds to the radius range of a rabbit heart. The inset shows the photograph bending demonstration of the device on the outer surface of a cylinder (white scale bar: 5 mm). (**B**) The change in the transistor signal on repetitive bending cycles.

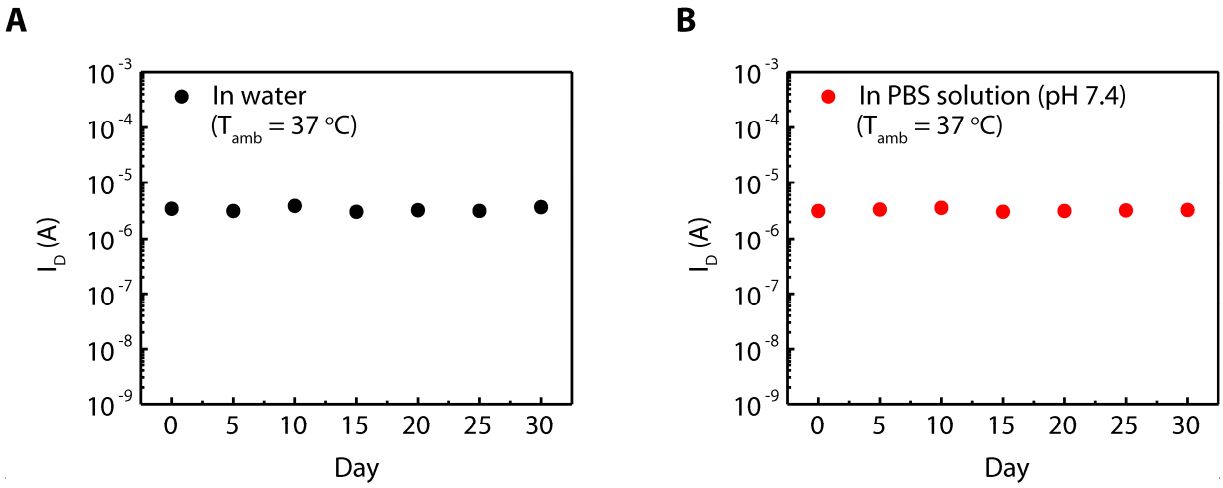

Fig. S3. Long-term stability test of the encapsulation characteristics. Electrical readout of the air-dielectric transistor of our epicardial patch during the immersing test in (**A**) water and (**B**) PBS (pH 7.4) for 30 days, respectively (V_G = 15 V, V_D = 1 V).

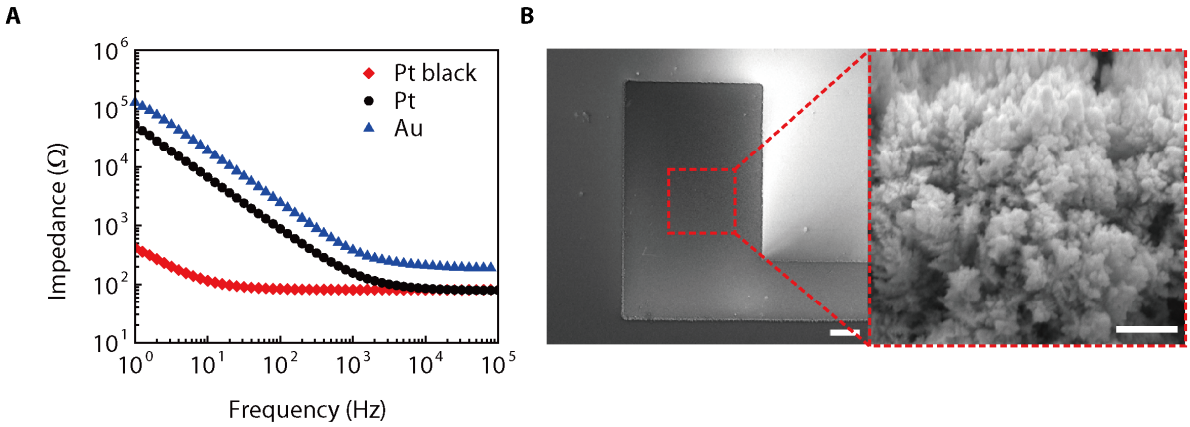

Fig. S4. Characterization of Pt black and other pacing electrode metals. (**A**) Impedance of three different pacing electrodes (Au, Pt, and Pt black) measured by electrochemical impedance spectroscopy (EIS). (**B**) Scanning electron microscope (SEM) image of the Pt black electrode (left, white scale bar: 100 μm). A magnified SEM image shows the formation of Pt nanoclusters at the pacing electrode surface (right, white scale bar: 400 nm).

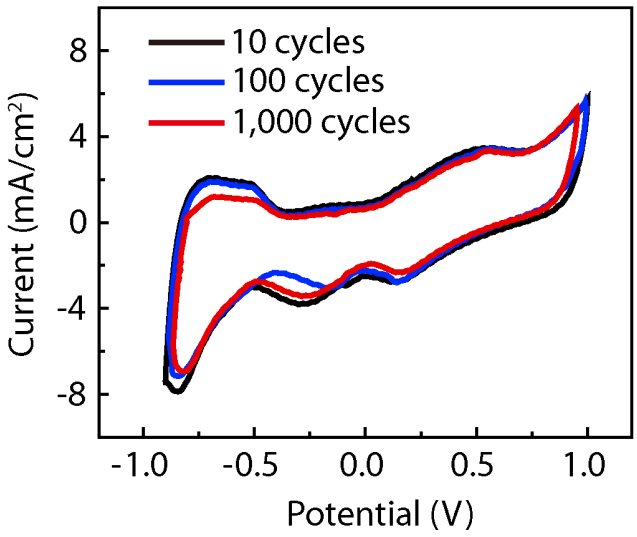

Fig. S5. Cyclic voltammograms of Pt black. Black, blue, and red cycle represent data for 10, 100, and 1,000 scanning cycles, respectively.

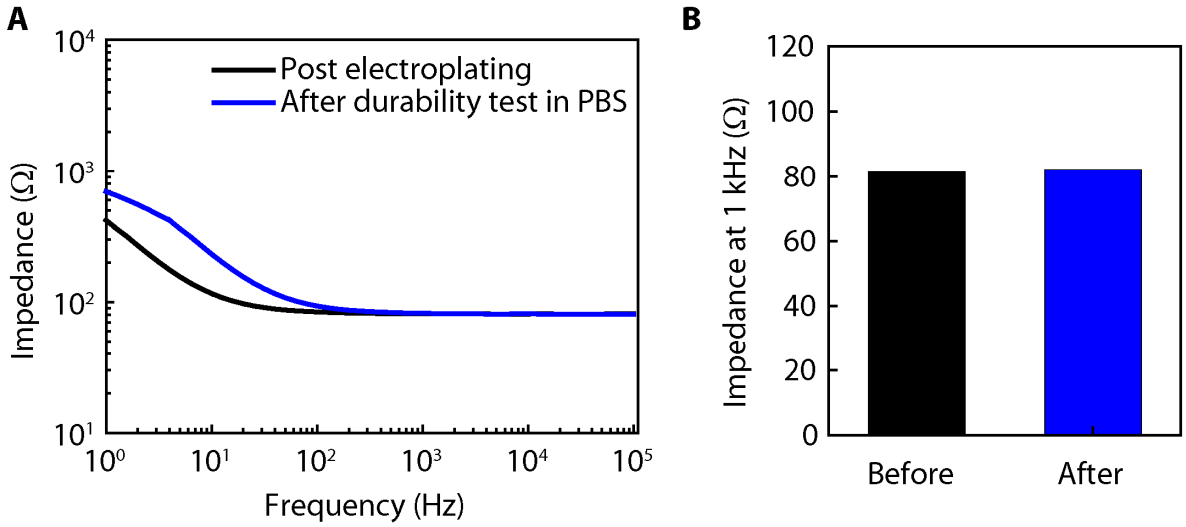

Fig. S6. Electrochemical stability of Pt black. (**A**) Impedance spectra of the Pt black electrode before and after durability test to an hour in PBS. For this durability test, the impedance measurement conducted after submerging it to an hour in PBS in an incubator at 37°C. (**B**) Impedance values before and after this durability test at 1 kHz. The impedance increased by 0.94% at 1 kHz after this durability test in PBS from the initial impedance of 81.37 **Ω**.

A

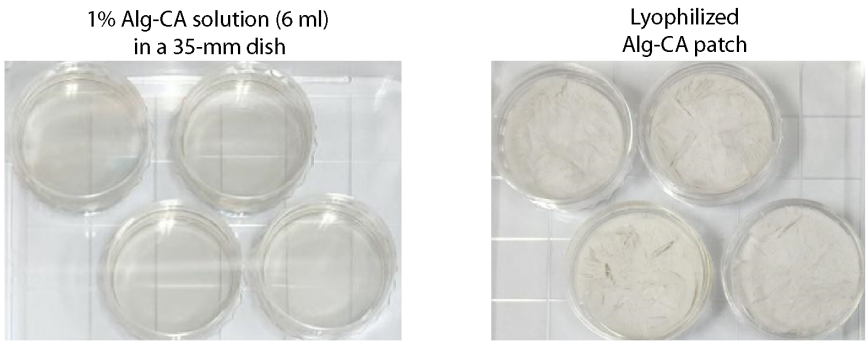

B

Patch #	Diameter (mm)	Thickness (mm)
Patch 1	33.52	0.98
Patch 2	33.47	0.98
Patch 3	34.61	1.00
Patch 4	34.49	1.03
Average	**34.02**	**0.998**
S.D.	**0.6098**	**0.0236**

Fig. S7. The fabrication reproducibility of Alg-CA patch. (**A**) The Alg-Ca patch images before and after lyophilize process in 35-mm dish. (**B**) Table of deviations in diameter and thickness of Alg-Ca patches according to the repeated fabrication.

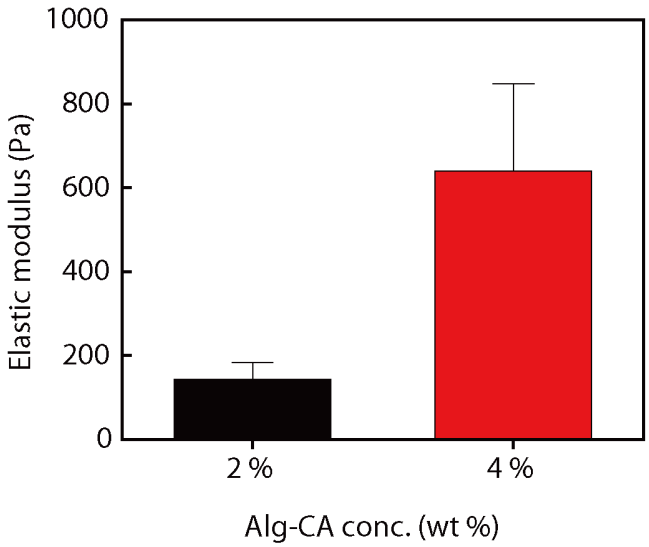

Fig. S8. Elastic modulus of bulk Alg-CA hydrogels. Elastic modulus with respect to Alg-CA concentration was tested.

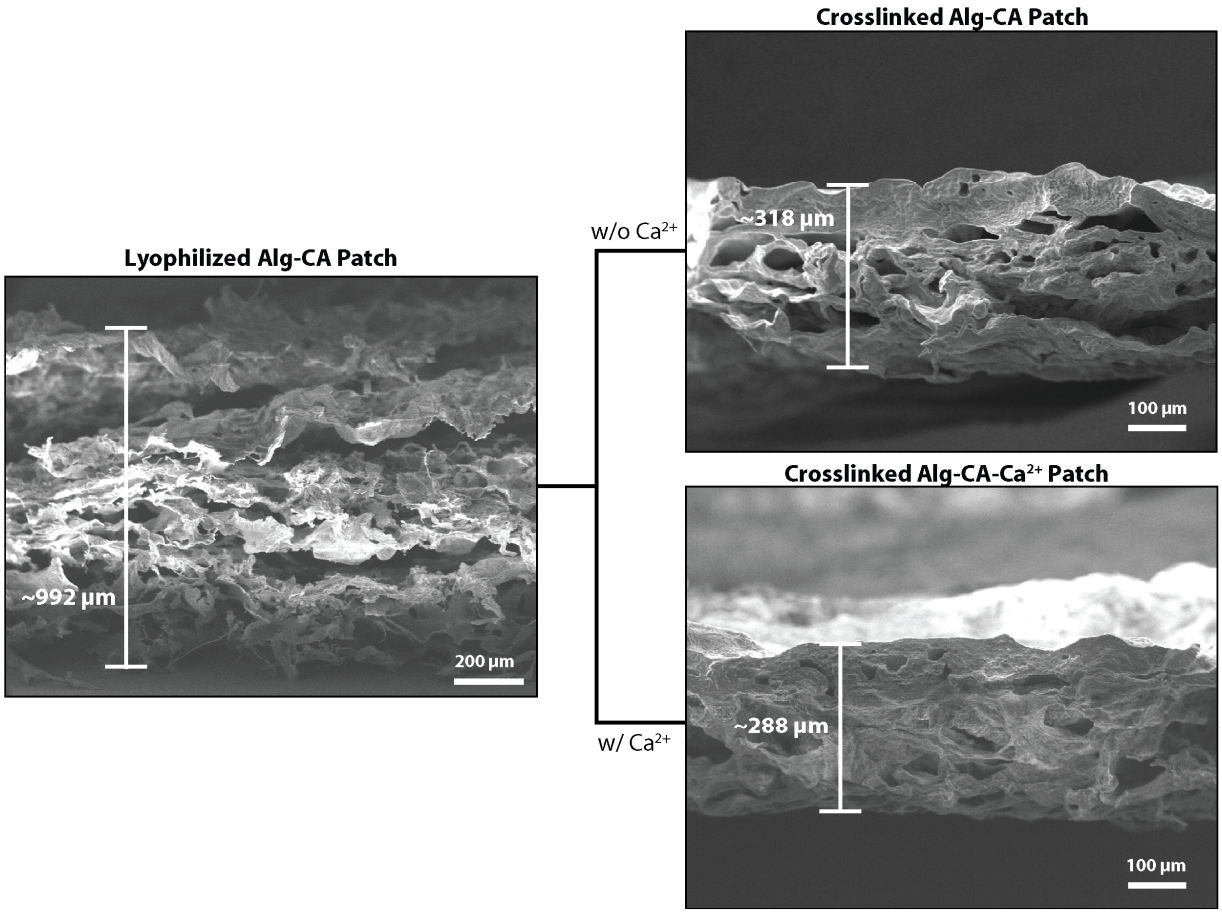

Fig. S9. Scanning electron microscope (SEM) images of hydrogel adhesive patch. Before and after crosslinking of lyophilized Alg-CA patches with and without Ca^{2+} treatment is shown.

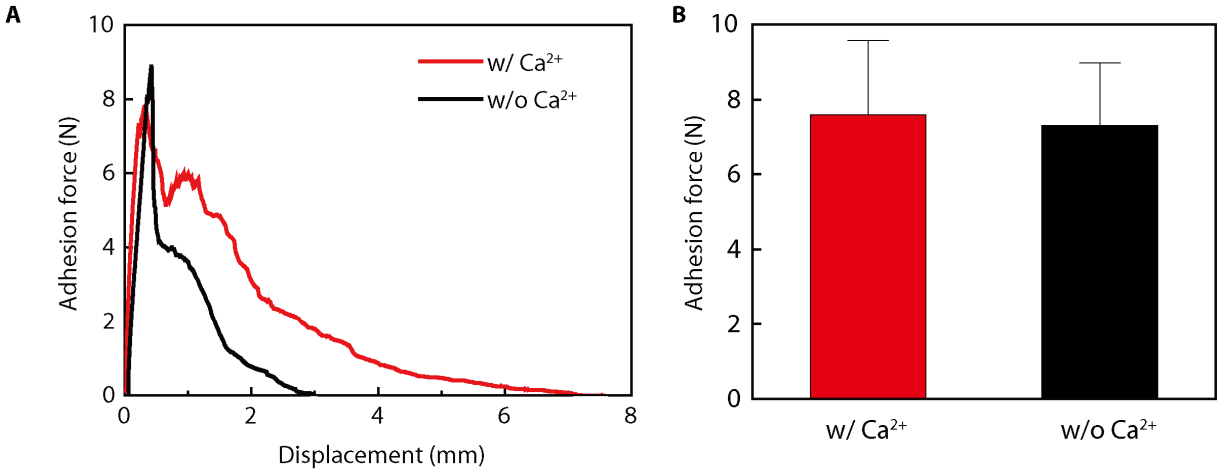

Fig. S10. Adhesion force of hydrogel adhesive layer. (**A**) The adhesion force with respect to displacement, with and without Ca^{2+} treatment. (**B**) Interfacial force of the adhesive patch with and without Ca^{2+}.

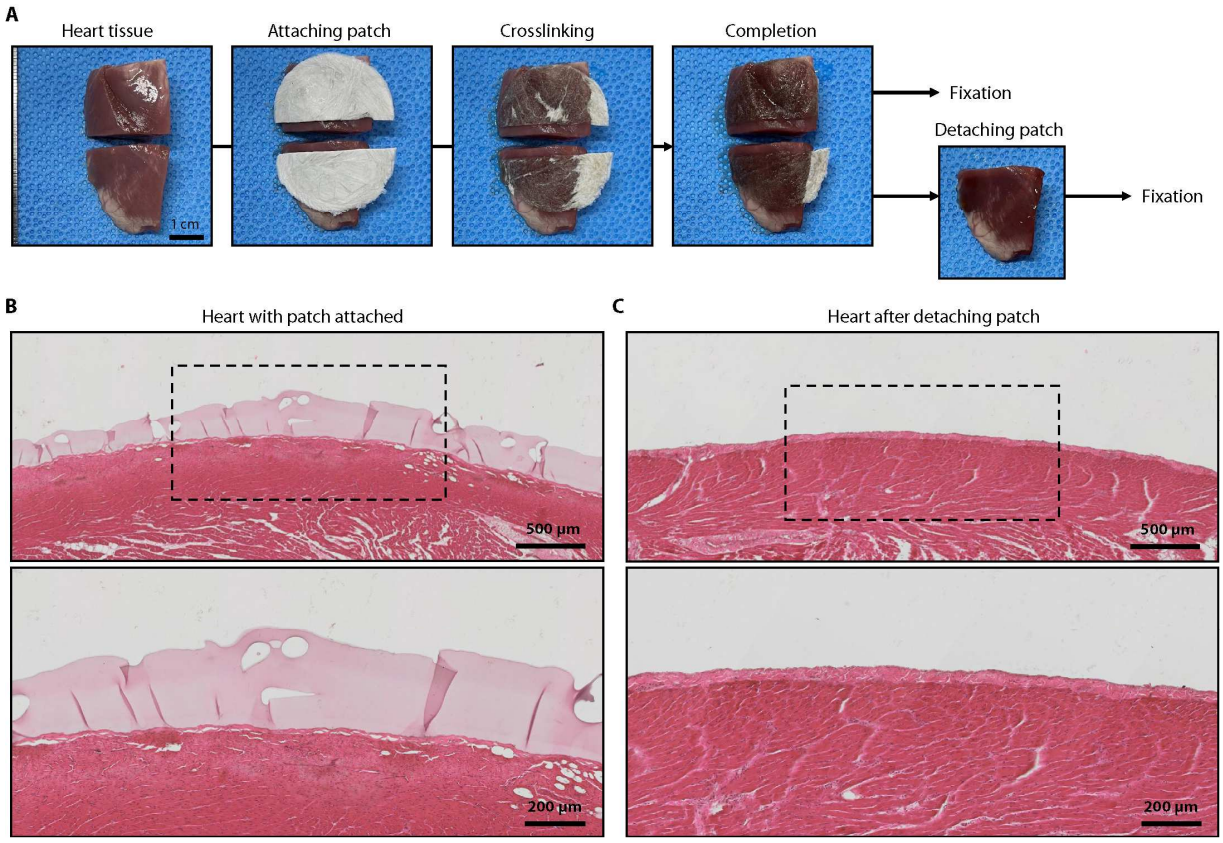

Fig. S11. Detach test of adhesive patch onto the heart tissue. (**A**) Detach test procedure onto a heart. H&E images of a heart surface (**B**) with the patch attachment, (**C**) after detaching this patch with no remnants of the adhesive and negligible damages (bottom images are magnified of black dash box of upper images).

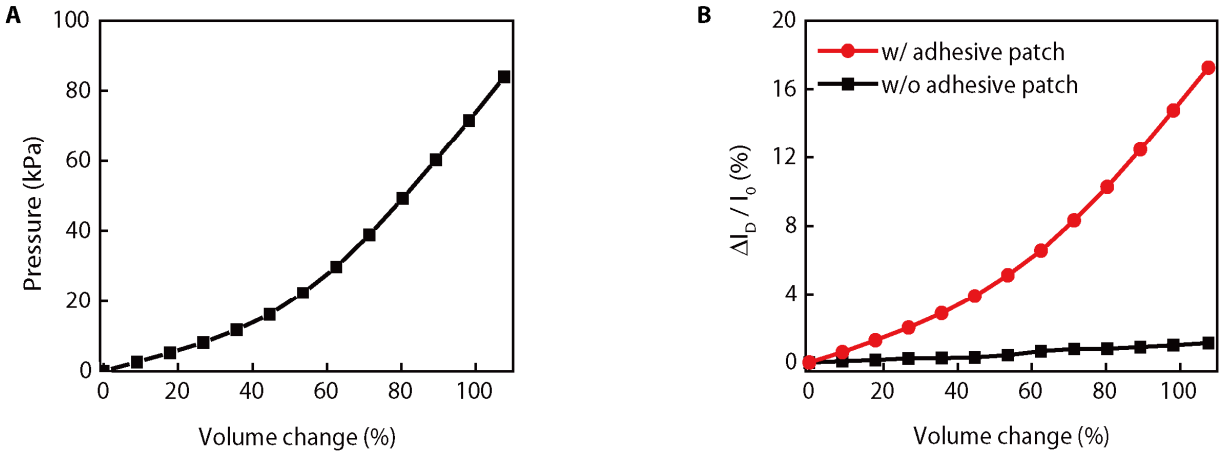

Fig. S12. Pressures and transistor signals ($\Delta I_D/I_0$) of the sensor with respect to the volume expansion of an artificial cardiac model. (**A**) The external pressure detected by a z-axis force gauge for varying the volume expansion of this artificial heart. (**B**) Relative change in I_D of the pressure-sensitive transistor by the volume of this artificial heart with and without the use of hydrogel adhesive layer.

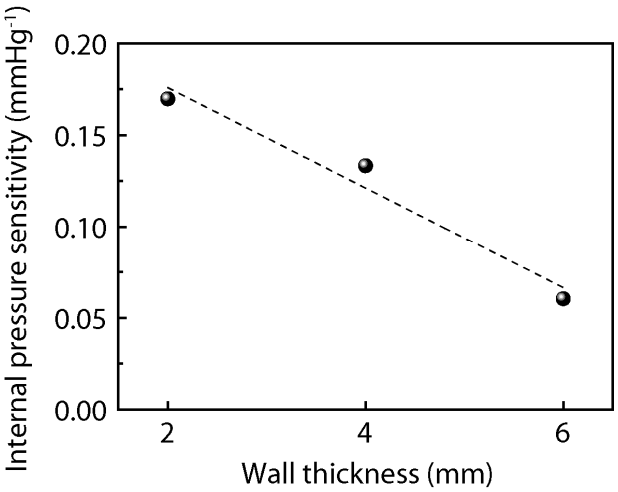

Fig. S13. Relationship of the wall thickness of an artificial heart and the internal pressure sensitivity. The dash line is the linear fit of this relationship.

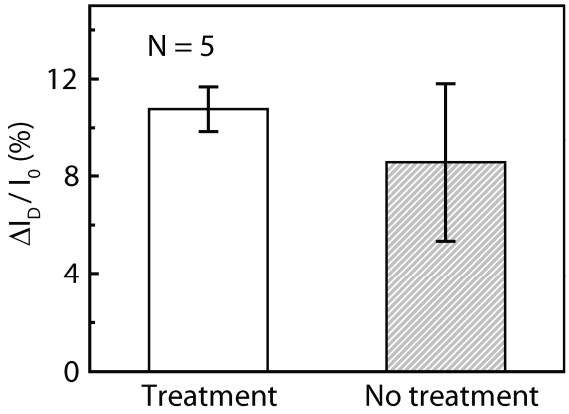

Fig. S14. Readout measurement stability data. Readout of the cardiac surface pressure at diastolic phase with or without the esmolol treatment during the patch device attachment onto the left ventricular surface.

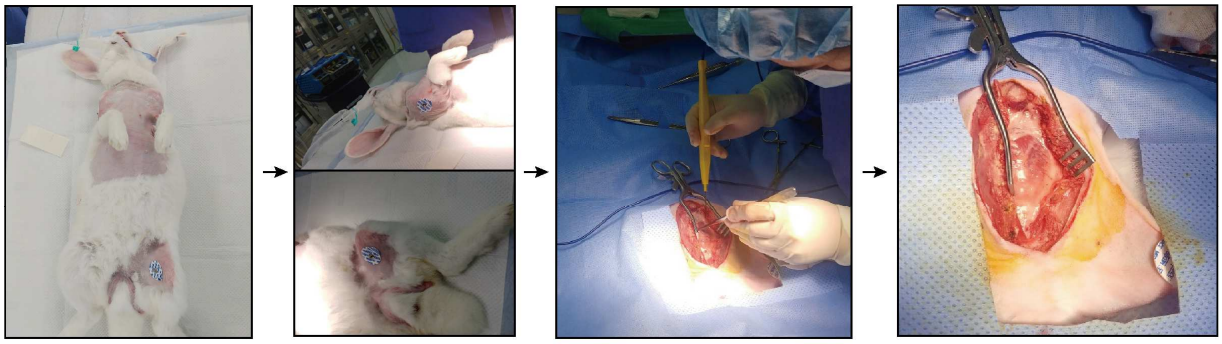

Fig. S15. Photograph of in-vivo experiment. Chronological preparation procedures of the in-vivo experiment using a live rabbit.

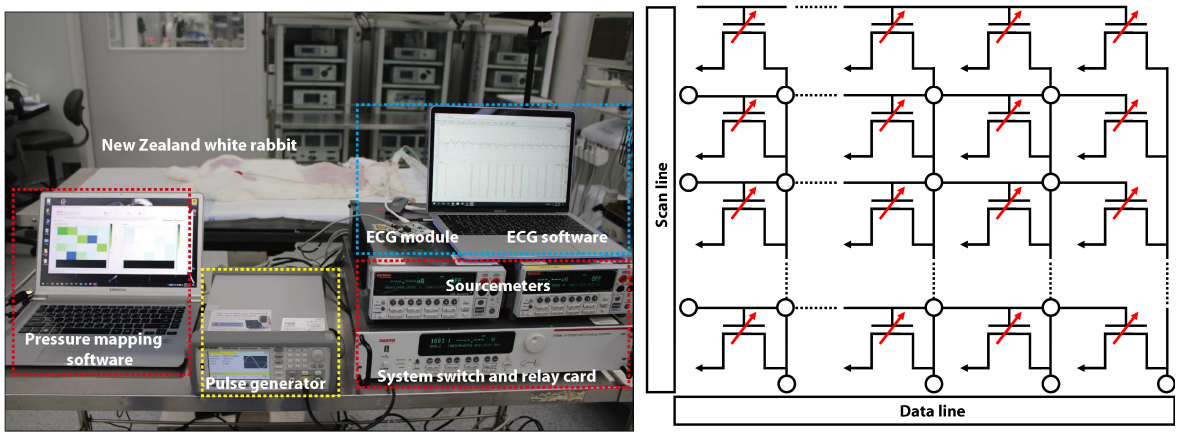

Fig. S16. Experimental equipment setup for the real-time monitoring system using a New Zealand white rabbit. (Left) The red and blue dotted boxes represent the data acquisition system for mechanophysiological sensing and ECG sensing, respectively. The yellow dotted box represents the pulse generator used to stimulate electrical pulses. (Right) The circuit diagram of the 10 × 10 pressure-sensitive transistor array.

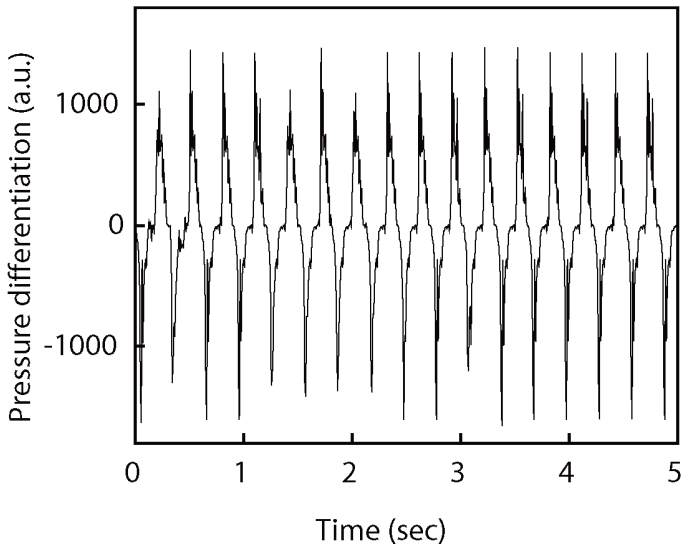

Fig. S17. Pressure differentiation data. Differential plot of the epicardial pressure recording data during cardiac beating motions.

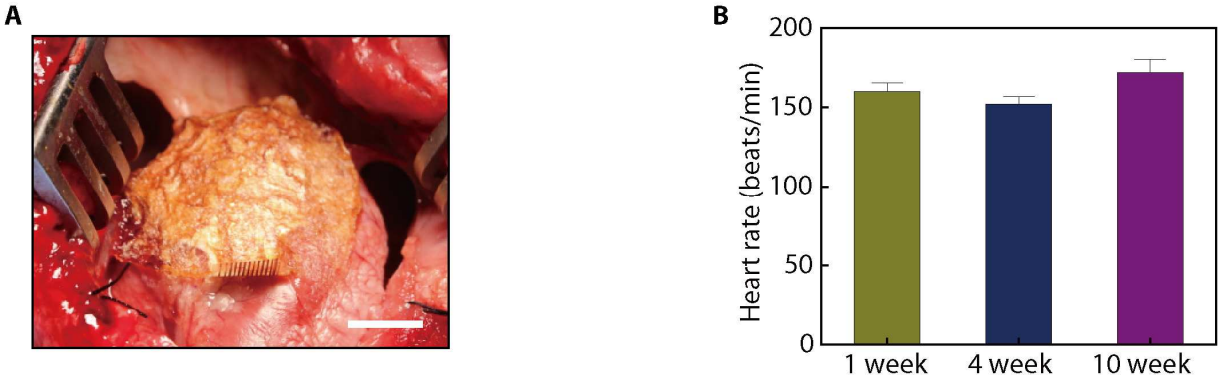

Fig. S18. Change in the heart rates of live rabbit after epicardial implantation of device platform for over 10 weeks. (**A**) Photograph of the device platform implanted on the epicardial surface (white scale bar: 10 mm). (**B**) The change in heart rates of the anesthetized rabbit for 10 weeks.

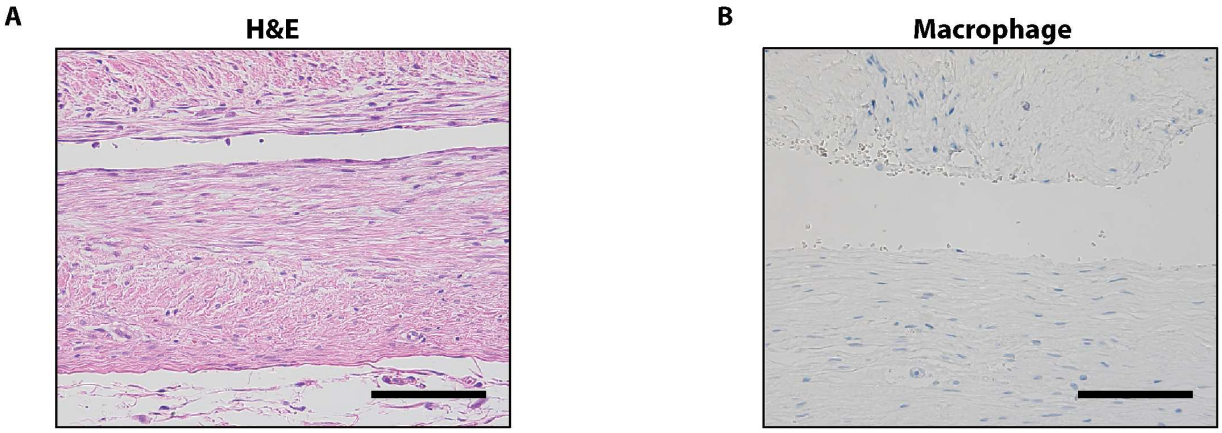

Fig. S19. In-vivo biocompatibility test of the device platform. (**A**) Representative hematoxylin and eosin (H&E) stained image and (**B**) macrophage assay (CD68 antibody) from subcutaneous tissue surrounding the heart, which was inserted with this device for 10 weeks (black scale bars: 100 μm).

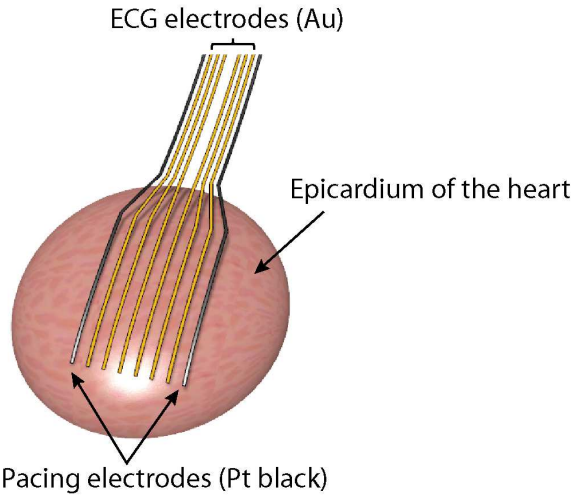

Fig. S20. Schematic illustration of a flexible epicardial patch. Flexible epicardial patch device with Cr/Au electrodes and Pt black electrodes for epicardial ECG recording and electrical pacing, respectively.

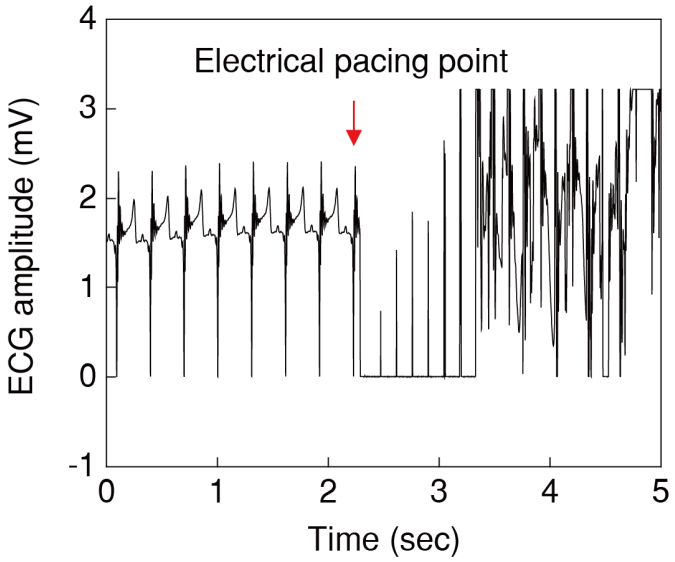

Fig. S21. Generation of ECG signal artifact. ECG signal artifact by electrical pacing pulses in the flexible epicardial patch with multiple electrodes.

A

B

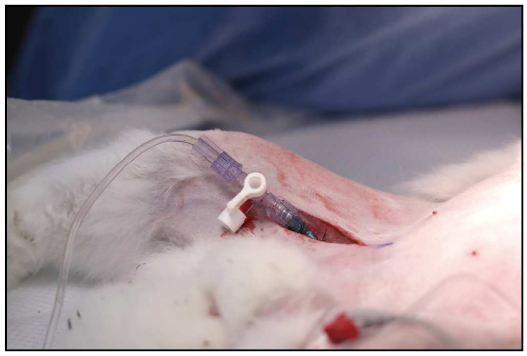

Fig. S22. Photographs of the peripheral blood flow recording setup to measure the frequency of heartbeat modulation. (**A**) Photograph of the PPG sensor fixed on the sublingual artery of the rabbit tongue. (**B**) Photograph of femoral insertion to measure arterial blood pressure.

Table S1. Comparison with recent and representative functional cardiac patch devices.

Functions	Physiological methods	Type of sensors	Characteristics	Limitations	Ref.
Monitoring	Electrophysiology	ECG (Transistor)	• Spatiotemporal mapping • High resolution • Low bending stiffness	• No treatment functions • Electrical interference • No wireless communication	(*14*)
		ECG (Transistor)	• Spatiotemporal mapping • Leakage free		(*15*)
		ECG (Electrode)	• Spatiotemporal mapping • Robust contact to epicardium		(*18*)
Treatment			• Bioresorbable • Wireless energy transfer • Electrical pacing	• No diagnosis functions	(*19*)
			• Wireless and battery-free • Multimodal pacing		(20)
Monitoring and treatment	Electrophysiology	ECG (Electrode) Temperature (Resistor) Strain (Piezoresistive)	• Spatiotemporal mapping • Multifunction sensing • Robust contact to epicardium	• Electrical interference • No wireless communication	(*12*)
		ECG (Electrode) Strain (Piezoresistive) Temperature (Resistor) pH sensor (Iridium oxide)	• Multiparametric physiological mapping and actuator		(*13*)
In-situ monitoring and treatment (In this work)	Mechanophysiology	Pressure sensor (Transistor)	• Simultaneous detecting and treatment (No electrical interference) • Mechanical analysis of cardiac activity • Spatiotemporal mapping	• No wireless communication	-

Table S2. Comparison with pressure sensors for biomedical applications.

Sensing Type	Properties	Sensitivity	SNR	Detection Range	Ref.
Capacitive	[Advantages] - Simple device structure [Disadvantages] - Neighboring interference - Low contrast ratio - Crosstalk effect	0.137 kPa^{-1}	506 (@ 0.5 kPa)	50 Pa to 6 kPa	(*73*)
		0.7 kPa^{-1} (<1 kPa) 0.13 kPa^{-1} (<10 kPa)	-	12 Pa to 430 kPa	(*74*)
		0.76 kPa^{-1} (<2 kPa) 0.11 kPa^{-1} (>2 kPa)	-	3 Pa to 20 kPa	(*75*)
		10.13 MPa^{-1} (<100 kPa)	-	16 mg to 600 kPa	(*76*)
		7.70 kPa^{-1}	-	13 Pa to 7.4 kPa	(*77*)
Piezoresistive	[Advantages] - Fast response time [Disadvantages] - Pyroelectric - Low contrast ratio - Crosstalk effect	0.76 kPa^{-1}	1101 (@ 2 kPa)	1.7 Pa to 6 kPa	(78)
		41.0 MPa^{-1}	-	10 kPa to 500 kPa	(79)
		0.48 kPa^{-1}	-	1.5 kPa to 6.5 kPa	(*80*)
Pressure-sensitive transistor (In this work)	[Advantages] - Active matrix - High array uniformity - High spatial contrast [Disadvantages] - Complicated layout	0.23 kPa^{-1}	13 (@ 1 kPa)	77 Pa to 200 kPa	-

Movie S1.

Spatiotemporal mapping of epicardial pressure distributions and the surface ECG trace during normal cardiac beatings. This movie is played slowly at 70% of the actual heart beating.

Movie S2.

Real-time spatiotemporal mapping of epicardial pressure distributions and the surface ECG trace during the bradycardia beating motion with successive electrical stimulation.

REFERENCES AND NOTES

1. S. S. Virani, A. Alonso, E. J. Benjamin, M. S. Bittencourt, C. W. Callaway, A. P. Carson, A. M. Chamberlain, A. R. Chang, S. Cheng, F. N. Delling, L. Djousse, M. S. V. Elkind, J. F. Ferguson, M. Fornage, S. S. Khan, B. M. Kissela, K. L. Knutson, T. W. Kwan, D. T. Lackland, T. T. Lewis, J. H. Lichtman, C. T. Longenecker, M. S. Loop, P. L. Lutsey, S. S. Martin, K. Matsushita, A. E. Moran, M. E. Mussolino, A. M. Perak, W. D. Rosamond, G. A. Roth, U. K. A. Sampson, G. M. Satou, E. B. Schroeder, S. H. Shah, C. M. Shay, N. L. Spartano, A. Stokes, D. L. Tirschwell, L. B. VanWagner, C. W. Tsao; American Heart Association Council on Epidemiology and Prevention Statistics Committee and Stroke Statistics Subcommittee, Heart disease and stroke statistics—2020 Update: A report from the American Heart Association. *Circulation* **141**, e139–e596 (2020).

2. A. S. Adabag, R. V. Luepker, V. L. Roger, B. J. Gersh, Sudden cardiac death: Epidemiology and risk factors. *Nat. Rev. Cardiol.* **7**, 216–225 (2010).

3. D. P. Zipes, H. J. J. Wellens, Sudden cardiac death. *Circulation* **98**, 2334–2351 (1998).

4. R. Mehra, Global public health problem of sudden cardiac death. *J. Electrocardiol.* **40**, S118–S122 (2007).

5. M. T. Keating, M. C. Sanguinetti, Molecular and cellular mechanisms of cardiac arrhythmias. *Cell* **104**, 569–580 (2001).

6. Task Force of the European Society of Cardiology the North American Society of Pacing Electrophysiology, Heart rate variability. *Circulation* **93**, 1043–1065 (1996).

7. A. J. Moss, W. J. Hall, D. S. Cannom, J. P. Daubert, S. L. Higgins, H. Klein, J. H. Levine, S. Saksena, A. L. Waldo, D. Wilber, M. W. Brown, M. Heo, Improved survival with an implanted defibrillator in patients with coronary disease at high risk for ventricular arrhythmia. *N. Engl. J. Med.* **335**, 1933–1940 (1996).

8. A. Mediratta, K. Addetia, M. Yamat, J. D. Moss, H. M. Nayak, M. C. Burke, L. Weinert, F. Maffessanti, V. Jeevanandam, V. Mor-Avi, R. M. Lang, 3D echocardiographic location of

implantable device leads and mechanism of associated tricuspid regurgitation. *JACC Cardiovasc. Imaging* **7**, 337–347 (2014).

9. K. A. Polyzos, A. A. Konstantelias, M. E. Falagas, Risk factors for cardiac implantable electronic device infection: A systematic review and meta-analysis. *Europace* **17**, 767–777 (2015).

10. P. B. Nery, R. Fernandes, G. M. Nair, G. L. Sumner, C. S. Ribas, S. M. D. Menon, X. Wang, A. D. Krahn, C. A. Morillo, S. J. Connolly, J. S. Healey, Device-related infection among patients with pacemakers and implantable defibrillators: Incidence, risk factors, and consequences. *J. Cardiovasc. Electrophysiol.* **21**, 786–790 (2010).

11. X. Mei, K. Cheng, Recent development in therapeutic cardiac patches. *Front. Cardiovasc. Med.* **7**, 610364 (2020).

12. D.-H. Kim, R. Ghaffari, N. Lu, S. Wang, S. P. Lee, H. Keum, R. D'Angelo, L. Klinker, Y. Su, C. Lu, Y.-S. Kim, A. Ameen, Y. Li, Y. Zhang, B. de Graff, Y.-Y. Hsu, Z. Liu, J. Ruskin, L. Xu, C. Lu, F. G. Omenetto, Y. Huang, M. Mansour, M. J. Slepian, J. A. Rogers, Electronic sensor and actuator webs for large-area complex geometry cardiac mapping and therapy. *Proc. Natl. Acad. Sci. U.S.A.* **109**, 19910–19915 (2012).

13. L. Xu, S. R. Gutbrod, A. P. Bonifas, Y. Su, M. S. Sulkin, N. Lu, H.-J. Chung, K.-I. Jang, Z. Liu, M. Ying, C. Lu, R. C. Webb, J.-S. Kim, J. I. Laughner, H. Cheng, Y. Liu, A. Ameen, J.-W. Jeong, G.-T. Kim, Y. Huang, I. R. Efimov, J. A. Rogers, 3D multifunctional integumentary membranes for spatiotemporal cardiac measurements and stimulation across the entire epicardium. *Nat. Commun.* **5**, 3329 (2014).

14. J. Viventi, D.-H. Kim, J. D. Moss, Y.-S. Kim, J. A. Blanco, N. Annetta, A. Hicks, J. Xiao, Y. Huang, D. J. Callans, J. A. Rogers, B. Litt, A conformal, bio-Interfaced class of silicon electronics for mapping cardiac electrophysiology. *Sci. Transl. Med.* **2**, 24ra22 (2010).

15. H. Fang, K. J. Yu, C. Gloschat, Z. Yang, E. Song, C.-H. Chiang, J. Zhao, S. M. Won, S. Xu, M. Trumpis, Y. Zhong, S. W. Han, Y. Xue, D. Xu, S. W. Choi, G. Cauwenberghs, M. Kay, Y. Huang, J.

Viventi, I. R. Efimov, J. A. Rogers, Capacitively coupled arrays of multiplexed flexible silicon transistors for long-term cardiac electrophysiology. *Nat. Biomed. Eng.* **1**, 0038 (2017).

16. J. Park, S. Choi, A. H. Janardhan, S.-Y. Lee, S. Raut, J. Soares, K. Shin, S. Yang, C. Lee, K.-W. Kang, H. R. Cho, S. J. Kim, P. Seo, W. Hyun, S. Jung, H.-J. Lee, N. Lee, S. H. Choi, M. Sacks, N. Lu, M. E. Josephson, T. Hyeon, D.-H. Kim, H. J. Hwang, Electromechanical cardioplasty using a wrapped elasto-conductive epicardial mesh. *Sci. Transl. Med.* **8**, 344ra86 (2016).

17. S.-H. Sunwoo, S. I. Han, H. Kang, Y. S. Cho, D. Jung, C. Lim, C. Lim, M. Cha, S.-P. Lee, T. Hyeon, D.-H. Kim, Stretchable low-impedance nanocomposite comprised of Ag–Au Core–shell nanowires and Pt black for epicardial recording and stimulation. *Adv. Mater. Technol.* **5**, 1900768 (2020).

18. J. Liu, X. Zhang, Y. Liu, M. Rodrigo, P. D. Loftus, J. Aparicio-Valenzuela, J. Zheng, T. Pong, K. J. Cyr, M. Babakhanian, J. Hasi, J. Li, Y. Jiang, C. J. Kenney, P. J. Wang, A. M. Lee, Z. Bao, Intrinsically stretchable electrode array enabled in vivo electrophysiological mapping of atrial fibrillation at cellular resolution. *Proc. Natl. Acad. Sci. U.S.A.* **117**, 14769–14778 (2020).

19. Y. S. Choi, R. T. Yin, A. Pfenniger, J. Koo, R. Avila, K. B. Lee, S. W. Chen, G. Lee, G. Li, Y. Qiao, A. Murillo-Berlioz, A. Kiss, S. Han, S. M. Lee, C. Li, Z. Xie, Y.-Y. Chen, A. Burrell, B. Geist, H. Jeong, J. Kim, H.-J. Yoon, A. Banks, S.-K. Kang, Z. J. Zhang, C. R. Haney, A. V. Sahakian, D. Johnson, T. Efimova, Y. Huang, G. D. Trachiotis, B. P. Knight, R. K. Arora, I. R. Efimov, J. A. Rogers, Fully implantable and bioresorbable cardiac pacemakers without leads or batteries. *Nat. Biotechnol.* **39**, 1228–1238 (2021).

20. P. Gutruf, R. T. Yin, K. B. Lee, J. Ausra, J. A. Brennan, Y. Qiao, Z. Xie, R. Peralta, O. Talarico, A. Murillo, S. W. Chen, J. P. Leshock, C. R. Haney, E. A. Waters, C. Zhang, H. Luan, Y. Huang, G. Trachiotis, I. R. Efimov, J. A. Rogers, Wireless, battery-free, fully implantable multimodal and multisite pacemakers for applications in small animal models. *Nat. Commun.* **10**, 5742 (2019).

21. A. Baranchuk, J. Kang, C. Shaw, D. Campbell, S. Ribas, W. M. Hopman, H. Alanazi, D. P. Redfearn, C. S. Simpson, Electromagnetic interference of communication devices on ECG machines. *Clin. Cardiol.* **32**, 588–592 (2009).

22. M. T. Liaquat, I. Ahmed, T. Alzahrani, *Pacemaker Malfunction* (StatPearls Publishing, 2022); https://ncbi.nlm.nih.gov/books/NBK553149/.

23. E. Cingolani, J. I. Goldhaber, E. Marbán, Next-generation pacemakers: From small devices to biological pacemakers. *Nat. Rev. Cardiol.* **15**, 139–150 (2018).

24. B. Nowak, Pacemaker stored electrograms: Teaching us what is really going on in our patients. *Pacing Clin. Electrophysiol.* **25**, 838–849 (2002).

25. C. Holmgren, T. Carlsson, C. Mannheimer, N. Edvardsson, Risk of interference from transcutaneous electrical nerve stimulation on the sensing function of implantable defibrillators. *Pacing Clin. Electrophysiol.* **31**, 151–158 (2008).

26. T. Shishido, M. Sugimachi, O. Kawaguchi, H. Miyano, T. Kawada, W. Matsuura, Y. Ikeda, T. Sato, J. Alexander, K. Sunagawa, A new method to measure regional myocardial time-varying elastance using minute vibration. *Am. J. Physiol.* **274**, H1404–H1415 (1998).

27. M. Han, L. Chen, K. Aras, C. Liang, X. Chen, H. Zhao, K. Li, N. R. Faye, B. Sun, J.-H. Kim, W. Bai, Q. Yang, Y. Ma, W. Lu, E. Song, J. M. Baek, Y. Lee, C. Liu, J. B. Model, G. Yang, R. Ghaffari, Y. Huang, I. R. Efimov, J. A. Rogers, Catheter-integrated soft multilayer electronic arrays for multiplexed sensing and actuation during cardiac surgery. *Nat. Biomed. Eng.* **4**, 997–1009 (2020).

28. E. T. Roche, M. A. Horvath, I. Wamala, A. Alazmani, S.-E. Song, W. Whyte, Z. Machaidze, C. J. Payne, J. C. Weaver, G. Fishbein, J. Kuebler, N. V. Vasilyev, D. J. Mooney, F. A. Pigula, C. J. Walsh, Soft robotic sleeve supports heart function. *Sci. Transl. Med.* **9**, eaaf3925 (2017).

29. M. Naveed, L. Han, G. J. Khan, S. Yasmeen, R. Mikrani, M. Abbas, L. Cunyu, Z. Xiaohui, Cardio-supportive devices (VRD & DCC device) and patches for advanced heart failure: A review, summary of state of the art and future directions. *Biomed. Pharmacother.* **102**, 41–54 (2018).

30. J. Jang, H. Kim, S. Ji, H. J. Kim, M. S. Kang, T. S. Kim, J. Won, J.-H. Lee, J. Cheon, K. Kang, W. B. Im, J.-U. Park, Mechanoluminescent, air-dielectric MoS_2 transistors as active-matrix pressure sensors for wide detection ranges from footsteps to cellular motions. *Nano Lett.* **20**, 66–74 (2020).

31. S. Ji, J. Jang, J. C. Hwang, Y. Lee, J.-H. Lee, J.-U. Park, Amorphous oxide semiconductor transistors with air dielectrics for transparent and wearable pressure sensor arrays. *Adv. Mater. Technol.* **5**, 1900928 (2020).

32. S.-H. Shin, S. Ji, S. Choi, K.-H. Pyo, B. Wan An, J. Park, J. Kim, J.-Y. Kim, K.-S. Lee, S.-Y. Kwon, J. Heo, B.-G. Park, J.-U. Park, Integrated arrays of air-dielectric graphene transistors as transparent active-matrix pressure sensors for wide pressure ranges. *Nat. Commun.* **8**, 14950 (2017).

33. J. Jang, B. Oh, S. Jo, S. Park, H. S. An, S. Lee, W. H. Cheong, S. Yoo, J.-U. Park, Human-interactive, active-matrix displays for visualization of tactile pressures. *Adv. Mater. Technol.* **4**, 1900082 (2019).

34. W. H. Cheong, B. Oh, S.-H. Kim, J. Jang, S. Ji, S. Lee, J. Cheon, S. Yoo, S.-Y. Lee, J.-U. Park, Platform for wireless pressure sensing with built-in battery and instant visualization. *Nano Energy* **62**, 230–238 (2019).

35. A. Moarabi, B. Mosallanejad, A. R. Ghadiri, R. Avizeh, Radiographic measurement of vertebral heart scale (VHS) in New Zealand white rabbits. *Iran. J. Vet. Surg.* **10**, 37–42 (2015).

36. L. Blanc, A. Delchambre, P. Lambert, Flexible medical devices: Review of controllable stiffness solutions. *Actuators* **6**, 23 (2017).

37. K. Bazaka, M. V. Jacob, Implantable devices: Issues and challenges. *Electronics* **2**, 1–34 (2013).

38. C. D. Swerdlow, W. H. Olson, M. E. O'Connor, D. M. Gallik, R. A. Malkin, M. Laks, Cardiovascular collapse caused by electrocardiographically silent 60-Hz intracardiac leakage current. *Circulation* **99**, 2559–2564 (1999).

39. M. M. Laks, R. Arzbaecher, J. J. Bailey, D. B. Geselowitz, A. S. Berson, Recommendations for safe current limits for electrocardiographs. *Circulation* **93**, 837–839 (1996).

40. Amendment of recommendations for standardization of specifications for instruments in electrocardiography and vectorcardiography concerning safety and electrical shock hazards. *IEEE Trans. Biomed. Eng.* **20**, 140–141 (1973).

41. Y. H. Kim, G. H. Kim, M. S. Kim, S.-D. Jung, Iridium oxide–electrodeposited nanoporous gold multielectrode array with enhanced stimulus efficacy. *Nano Lett.* **16**, 7163–7168 (2016).

42. J. Shin, J. S. Lee, C. Lee, H.-J. Park, K. Yang, Y. Jin, J. H. Ryu, K. S. Hong, S.-H. Moon, H.-M. Chung, H. S. Yang, S. H. Um, J.-W. Oh, D.-I. Kim, H. Lee, S.-W. Cho, Tissue adhesive catechol-modified hyaluronic acid hydrogel for effective, minimally invasive cell therapy. *Adv. Funct. Mater.* **25**, 3814–3824 (2015).

43. J. H. Ryu, J. S. Choi, E. Park, M. R. Eom, S. Jo, M. S. Lee, S. K. Kwon, H. Lee, Chitosan oral patches inspired by mussel adhesion. *J. Control. Release* **317**, 57–66 (2020).

44. R. Wang, J. Li, W. Chen, T. Xu, S. Yun, Z. Xu, Z. Xu, T. Sato, B. Chi, H. Xu, A biomimetic mussel-inspired ε-poly-l-lysine hydrogel with robust tissue-anchor and anti-infection capacity. *Adv. Funct. Mater.* **27**, 1604894 (2017).

45. W. Zhang, R. Wang, Z. Sun, X. Zhu, Q. Zhao, T. Zhang, A. Cholewinski, F. (K.) Yang, B. Zhao, R. Pinnaratip, P. K. Forooshani, B. P. Lee, Catechol-functionalized hydrogels: Biomimetic design, adhesion mechanism, and biomedical applications. *Chem. Soc. Rev.* **49**, 433–464 (2020).

46. K. Y. Lee, D. J. Mooney, Alginate: Properties and biomedical applications. *Prog. Polym. Sci.* **37**, 106–126 (2012).

47. A. Cholewinski, F. (K.) Yang, B. Zhao, Algae–mussel-inspired hydrogel composite glue for underwater bonding. *Mater. Horiz.* **6**, 285–293 (2019).

48. J. Shin, S. Choi, J. H. Kim, J. H. Cho, Y. Jin, S. Kim, S. Min, S. K. Kim, D. Choi, S.-W. Cho, Tissue tapes—Phenolic hyaluronic acid hydrogel patches for off-the-shelf therapy. *Adv. Funct. Mater.* **29**, 1903863 (2019).

49. C. H. Yang, M. X. Wang, H. Haider, J. H. Yang, J.-Y. Sun, Y. M. Chen, J. Zhou, Z. Suo, Strengthening alginate/polyacrylamide hydrogels using various multivalent cations. *ACS Appl. Mater. Interfaces* **5**, 10418–10422 (2013).

50. J.-Y. Sun, X. Zhao, W. R. K. Illeperuma, O. Chaudhuri, K. H. Oh, D. J. Mooney, J. J. Vlassak, Z. Suo, Highly stretchable and tough hydrogels. *Nature* **489**, 133–136 (2012).

51. W. Hiesinger, M. J. Brukman, R. C. McCormick, J. R. Fitzpatrick III, J. R. Frederick, E. C. Yang, J. R. Muenzer, N. A. Marotta, M. F. Berry, P. Atluri, Y. J. Woo, Myocardial tissue elastic properties determined by atomic force microscopy after stromal cell–derived factor 1α angiogenic therapy for acute myocardial infarction in a murine model. *J. Thorac. Cardiovasc. Surg.* **143**, 962–966 (2012).

52. C. Larson, B. Peele, S. Li, S. Robinson, M. Totaro, L. Beccai, B. Mazzolai, R. Shepherd, Highly stretchable electroluminescent skin for optical signaling and tactile sensing. *Science* **351**, 1071–1074 (2016).

53. J. G. Jacot, J. C. Martin, D. L. Hunt, Mechanobiology of cardiomyocyte development. *J. Biomech.* **43**, 93–98 (2010).

54. A. H. Gradman, F. Alfayoumi, From left ventricular hypertrophy to congestive heart failure: Management of hypertensive heart disease. *Prog. Cardiovasc. Dis.* **48**, 326–341 (2006).

55. M. Nakamura, J. Sadoshima, Mechanisms of physiological and pathological cardiac hypertrophy. *Nat. Rev. Cardiol.* **15**, 387–407 (2018).

56. S. Gunther, W. Grossman, Determinants of ventricular function in pressure-overload hypertrophy in man. *Circulation* **59**, 679–688 (1979).

57. B. A. Carabello, Concentric versus eccentric remodeling. *J. Card. Fail.* **8**, S258–S263 (2002).

58. W. B. Kannel, T. Gordon, W. P. Castelli, J. R. Margolis, Electrocardiographic left ventricular hypertrophy and risk of coronary heart disease. The Framingham study. *Ann. Intern. Med.* **72**, 813–822 (1970).

59. J. Siegrist, R. Peter, W. Motz, B. E. Strauer, The role of hypertension, left ventricular hypertrophy and psychosocial risks in cardiovascular disease: Prospective evidence from blue-collar men. *Eur. Heart J.* **13**, 89–95 (1992).

60. G. Schillaci, P. Verdecchia, C. Porcellati, O. Cuccurullo, C. Cosco, F. Perticone, Continuous relation between left ventricular mass and cardiovascular risk in essential hypertension. *Hypertension* **35**, 580–586 (2000).

61. J. Sundström, L. Lind, J. Ärnlöv, B. Zethelius, B. Andrén, H. O. Lithell, Echocardiographic and electrocardiographic diagnoses of left ventricular hypertrophy predict mortality independently of each other in a population of elderly men. *Circulation* **103**, 2346–2351 (2001).

62. W. Grossman, L. P. Mclaurin, S. P. Moos, M. Stefadouros, D. T. Young, Wall thickness and diastolic properties of the left ventricle. *Circulation* **49**, 129–135 (1974).

63. J. A. Wisneski, J. D. Bristow, Left ventricular stiffness. *Annu. Rev. Med.* **29**, 475–483 (1978).

64. D. Wiest, Esmolol. A review of its therapeutic efficacy and pharmacokinetic characteristics. *Clin. Pharmacokinet.* **28**, 190–202 (1995).

65. R. A. B. Burton, J. E. Schneider, M. J. Bishop, P. W. Hales, C. Bollensdorff, M. D. Robson, K. C. K. Wong, J. Morris, T. A. Quinn, P. Kohl, Microscopic magnetic resonance imaging reveals high prevalence of third coronary artery in human and rabbit heart. *Europace* **14**, v73–v81 (2012).

66. J. T. Dodge, B. G. Brown, E. L. Bolson, H. T. Dodge, Lumen diameter of normal human coronary arteries. Influence of age, sex, anatomic variation, and left ventricular hypertrophy or dilation. *Circulation* **86**, 232–246 (1992).

67. S. Sieciński, P. S. Kostka, E. J. Tkacz, Heart rate variability analysis on electrocardiograms, seismocardiograms and gyrocardiograms on healthy volunteers. *Sensors* **20**, 4522 (2020).

68. R. Wégria, C. W. Frank, H.-H. Wang, J. Lammerant, The effect of atrial and ventricular tachycardia on cardiac output, coronary blood flow and mean arterial blood pressure. *Circ. Res.* **6**, 624–632 (1958).

69. K. K. Steinbach, O. Merl, K. Frohner, C. Hief, M. Nürnberg, W. Kaltenbrunner, A. Podczeck, E. Wessely, Hemodynamics during ventricular tachyarrhythmias. *Am. Heart J.* **127**, 1102–1106 (1994).

70. J. Handler, Adverse effects using combined rate-slowing antihypertensive agents. *J. Clin. Hypertens.* **13**, 529–532 (2011).

71. S. E. Stanca, F. Hänschke, A. Ihring, G. Zieger, J. Dellith, E. Kessler, H.-G. Meyer, Chemical and electrochemical synthesis of platinum black. *Sci. Rep.* **7**, 1074 (2017).

72. C. Lee, J. Shin, J. S. Lee, E. Byun, J. H. Ryu, S. H. Um, D.-I. Kim, H. Lee, S.-W. Cho, Bioinspired, calcium-free alginate hydrogels with tunable physical and mechanical properties and improved biocompatibility. *Biomacromolecules* **14**, 2004–2013 (2013).

73. L. A. Kurup, C. M. Cole, J. N. Arthur, S. D. Yambem, Graphene porous foams for capacitive pressure sensing. *ACS Appl. Nano Mater.* **5**, 2973–2983 (2022).

74. C. M. Boutry, Y. Kaizawa, B. C. Schroeder, A. Chortos, A. Legrand, Z. Wang, J. Chang, P. Fox, Z. Bao, A stretchable and biodegradable strain and pressure sensor for orthopaedic application. *Nat. Electron.* **1**, 314–321 (2018).

75. C. M. Boutry, A. Nguyen, Q. O. Lawal, A. Chortos, S. Rondeau-Gagné, Z. Bao, A sensitive and biodegradable pressure sensor array for cardiovascular monitoring. *Adv. Mater.* **27**, 6954–6961 (2015).

76. X. He, Z. Liu, G. Shen, X. He, J. Liang, Y. Zhong, T. Liang, J. He, Y. Xin, C. Zhang, D. Ye, G. Cai, Microstructured capacitive sensor with broad detection range and long-term stability for human activity detection. *npj Flex. Electron.* **5**, 17 (2021).

77. S. Gong, W. Schwalb, Y. Wang, Y. Chen, Y. Tang, J. Si, B. Shirinzadeh, W. Cheng, A wearable and highly sensitive pressure sensor with ultrathin gold nanowires. *Nat. Commun.* **5**, 3132 (2014).

78. S. Kim, Y. Dong, M. M. Hossain, S. Gorman, I. Towfeeq, D. Gajula, A. Childress, A. M. Rao, G. Koley, Piezoresistive graphene/P(VDF-TrFE) heterostructure based highly sensitive and flexible pressure sensor. *ACS Appl. Mater. Interfaces* **11**, 16006–16017 (2019).

79. Y. Jeong, J. Park, J. Lee, K. Kim, I. Park, Ultrathin, biocompatible, and flexible pressure sensor with a wide pressure range and its biomedical application. *ACS Sens.* **5**, 481–489 (2020).

80. L.-W. Lo, H. Shi, H. Wan, Z. Xu, X. Tan, C. Wang, Inkjet-printed soft resistive pressure sensor patch for wearable electronics applications. *Adv. Mater. Technol.* **5**, 1900717 (2020).